Temperature dependence of work hardening in sparsely twinning zirconium

Jaiveer Singh[1], S. Mahesh[2], Shomic Roy[1,3], Gulshan Kumar[1], D. Srivastava[4], G. K. Dey[4], N. Saibaba[5] and I. Samajdar[1]

[1]Department of Metallurgical Engineering & Materials Science, Indian Institute of Technology Bombay, Powai, Mumbai-400 076, India

[2]Departments of Aerospace Engineering, Indian Institute of Technology Madras, Chennai-600 036, India

[3]Scientific Services, Tata Steel Limited, Jamshedpur-831 001, India

[4]Materials Science Division, Bhabha Atomic Research Centre, Trombay, Mumbai-400 085, India

[5]Nuclear Fuel Complex, Hyderabad-500 062, India

Abstract

Fully recrystallized commercial Zirconium plates were subjected to uniaxial tension. Tests were conducted at different temperatures (123 K - 623 K) and along two plate directions. Both directions were nominally unfavorable for deformation twinning. The effect of the working temperature on crystallographic texture and in-grain misorientation development was insignificant. However, systematic variation in work hardening and in the area fraction and morphology of deformation twins was observed with temperature. At all temperatures, twinning was associated with significant near boundary mesoscopic shear, suggesting a possible linkage with twin nucleation. A binary tree based model of the polycrystal, which explicitly accounts for grain boundary accommodation and implements the phenomenological extended Voce hardening law, was implemented. This model could capture the measured stress-strain response and twin volume fractions accurately. Interestingly, slip and twin system hardness evolution permitted multiplicative decomposition into temperature-dependent, and accumulated strain-dependent parts. Furthermore, under conditions of relatively limited deformation twinning, the work hardening of the slip and twin systems followed two phenomenological laws proposed in the literature for non-twinning single-phase face centered cubic materials.

Keywords: Zirconium, Work hardening, Twinning, Polycrystal Plasticity, Temperature, Microstructure.

1. Introduction

Work hardening, which seeks to explain the mechanical response of materials under arbitrary loading paths, poses many important unresolved problems in materials science and engineering [1–4]. A detailed theory that builds up from the microscopic mechanisms and predicts the macroscopic stress-strain curve along a prescribed loading-path remains non-trivial. This has led to a search for reliable phenomenological work hardening models [4]. Among other aspects, such models seek to capture the influence of working temperature and strain-rate on material mechanical response. As early as 1953, it was recognized [5] that this dependence was controlled by a microscopic phenomenon termed dynamic recovery.

Slip and deformation twinning are accommodative microscopic mechanisms that are activated during plastic deformation in a number of materials. Both mechanisms are simultaneously activated in low stacking fault energy fcc (face centered cubic) materials, such as α −brass, and in hcp (hexagonal close packed) materials such as zirconium. While twinning does contribute to accommodate the imposed deformation, it is now well established [6–8] that the shear associated with deformation twinning accounts only for a small part of the imposed specimen deformation. Even so, the significance of deformation twins in material work hardening is great because of the interaction between twins and slip systems. Formation of deformation twins significantly alters the critical resolved shear stresses of slip systems in the grains, due to latent hardening, and reduction of the saturation stress of slip systems [8]. This, in turn, affects the spatial activation of slip processes markedly [9].

Work hardening models that account for both slip and deformation twinning are often built upon polycrystal plasticity models or crystal plasticity finite element models. In plastically deformed hcp Zircaloy-4, Lebensohn and Tomé [10] pioneered the application of polycrystal plasticity models to predict texture and mechanical response. Tomé et al. [11] applied the viscoplastic self-consistent model to explain the work hardening of uniaxially deformed specimens cut along both the in-plane and through thickness directions from a strongly textured zirconium plate. In order to fit the experimental work hardening response, they assumed a strong latent hardening interaction between each extension twinning system and all slip systems and all other twinning systems. Using this framework, Kaschner et al. [12] could explain the mechanical

response in pure zirconium during temperature change tests. Using distinct hardening parameters for the slip and twin systems at the two temperatures studied, they could capture the experimental mechanical response with the viscoplastic self-consistent polycrystal plasticity model. The internal variable controlling the hardening law of grains in [11,12] was the total accumulated slip and twinning shear in grains. Beyerlein and Tomé [13] proposed a model wherein dislocation densities were the internal variables. Temperature dependence enters into the Beyerlein and Tomé [13] model through the assumption of dislocation annihilation following the modified activation theory of Gilman [14]. Assuming that twin nucleation is thermally activated and therefore, probabilistic, and that twin propagation involves considerably less resistance than nucleation, the model of Beyerlein and Tomé [13] explains the temperature-dependent mechanical response under uniaxial loading both in-plane, and through the thickness of a clock rolled Zr sheet. An elastic-viscoplastic self-consistent model for Zircaloy capable of accounting for thermal strains was proposed by Qiao et al. [15]. A crystal plasticity finite element model of Zircaloy-2 incorporating both slip and twinning accommodation modes is due to Abdolvand et al. [16]. In this model, twins are not explicitly represented as parts of grains. Instead, a twin volume fraction is determined at each integration point, following a method similar to that used in the crystal plasticity models noted above. The twin volume evolves with deformation. Assuming the same deformation rate in both twin and matrix closes the system of equations at the integration point. As in the polycrystal plasticity models, slip-twin interactions are accounted for, using suitable latent hardening parameters.

Slip-twin interactions represent an important but complex aspect of polycrystal plasticity based work hardening models for hcp materials. While in [11,12,15,16], this interaction is modeled as a uniform latent hardening, a more complex scheme involving the intercept made on the slip direction by the twinning habit planes is adopted in Beyerlein and Tomé [13]. In contrast to all the aforementioned models, wherein twinned volumes are not explicitly represented, the conjugate grain model proposed by Proust et al. [17] treats twinned volumes as bands within the grains, deforming following compatibility conditions with the matrix. The interaction between twin and matrix in the physical grain, however, appears to be more complex than that suggested by Proust et al.'s simple compatibility condition [17,18].

It is clear from the foregoing, on one hand, that deformation twinning significantly affects the work hardening in hcp metals and alloys. Therefore, no simple relationship between the work hardening responses at different temperatures may be expected. On the other hand, a simple phenomenological work hardening model exists for fcc materials deforming by slip only, which adequately captures the temperature and strain-rate dependence of the work-hardening [4]. It is natural to ask if the temperature and strain-rate dependence of work hardening known in fcc materials will carry over to hcp polycrystalline materials, for the case of limited deformation twinning. It is the central objective of the present work to address this question.

In the present work, twinning is suppressed during uniaxial tension by loading samples cut from a highly textured Zircaloy-4 sheet along directions that are nominally unfavorable for extensive deformation twinning. The work hardening behaviour, texture and microstructure evolution in the temperature range of 123 K to 623 K has been characterized. Both yield stress and work hardening depend strongly on the working temperature [12,17,19–21] and on sample orientation or strain mode [20,22–25]. The experimental observations are interpreted through polycrystal plasticity modelling based on the binary tree model [26]. This model has been employed in previous works on Zircaloy-4 [22,27] also. The model directly accounts for the intergranular interactions, and grain boundary accommodation. It is found that for moderate volumes of deformation twinned regions, a surprisingly simple dependence of the hardness of slip and twinning systems in the grain bulk on temperature and accumulated strain is obtained: The slip system hardness can be multiplicatively decomposed into temperature-dependent and strain-dependent parts. Furthermore, the temperature dependent part follows a phenomenological scaling law proposed in the literature for fcc materials [4,28].

2. Experimental Method

In this study commercial Zirconium alloy (Zircaloy-4), rolled and then fully recrystallized sheet of 1.5 mm thickness, was used. The chemical composition of the Zircaloy-4 sheets is given in the Table 1. Tensile test specimens were prepared according to ASTM E8 standards in two different sample orientations (RD and TD). A range of working temperatures, 123 K to 623 K was used for direct and indirect observations. Tensile deformations were performed on servo-hydraulic Zwick-Roell^{TM} tensile testing machine at the strain rate of 5×10^{-4} mm/sec. Direct

observations were taken for the working temperatures of 123 K to 298 K. At 623 K temperature, direct observations on the specimen surface is not possible due to surface oxidation. The true stress-true strain ($\sigma - \varepsilon$) data were further analysed to extract information on work-hardening behaviours ($\frac{d\sigma}{d\varepsilon}$ versus σ). Interrupted tensile deformations, at different true strains, were used for detailed characterization for bulk texture and microstructural analysis.

Both X-ray diffraction and EBSD (electron backscattered diffraction) measurements were performed. For X-ray diffraction and microstructural characterization through EBSD, specimens were polished through standard metallography and electro-polishing in a 20:80 solution of perchloric acid and methanol by volume at -20°C and 20 volts dc [29]. For the latter, a Struers™ Lectopol system was used. All the microstructural measurements were made in the RD-TD section, containing rolling (RD) and transverse (TD) directions. The EBSD measurements were made on a FEI™ Quanta 3D-FEG (field emission gun) SEM (scanning electron microscopy), using TSL-OIM™ EBSD software. Multiple EBSD scans were made to cover large areas with identical beam and video conditions. EBSD measurements were done with step size of 0.2 μm. EBSD data above 0.1 CI (CI – confidence index is a statistical measure of automated indexing, $>$ 0.1 CI data representing > 95% success [30]) were taken for further analysis.

X-ray bulk textures of four incomplete (maximum tilt angle: 85°) pole figures ((0002), $(10\bar{1}0)$, $(10\bar{1}2)$, and $(10\bar{1}3)$) were measured on a PANalytical™ X'Pert PRO MRD system. A monochromatic Cu Kα beam of 2mm×2mm and Standard Schulz method in reflection mode [31] were used for these measurements. Combinations of highly accurate Eulerian cradle (0.0001° reproducibility) and multi-channel solid-state area detector (Pixel™) used for these pole figure measurements. ODFs were then calculated by inversion of the pole figures using the Arbitrarily Defined Cells (ADC) Method [32]. Commercial software, LaboTex from LaboSoft™, was used for the ODF calculations and plotting.

3. Modeling

Experimentally measured stress-strain curves were interpreted in polycrystal plasticity simulations using the binary-tree based model [26]. In this model, grains are treated as homogeneously deforming rigid-plastic rate-independent domains. Further, aggregates of grains

are represented as nodes of a binary tree, a standard data structure [33]. The lowest nodes of the binary tree represent grains. Higher binary tree nodes represent increasingly larger sub-aggregates of grains, culminating with the root of the tree (top most node). The root represents the entire polycrystalline aggregate. Following standard terminology [33], the two nodes $[l(k)]$ and $[r(k)]$ that are 'descended' from a certain 'parent' node $[k]$ in the binary tree are called its 'children'. The children $[l(k)]$ and $[r(k)]$ are then said to be 'siblings' of each other. The volume of the sub-aggregate represented by node $[k]$ will be denoted $w_{[k]}$ in the sequel. It follows that

$$w_{[k]} = w_{[l(k)]} + w_{[r(k)]}. \tag{1}$$

The binary tree representation of the microstructure is exemplified schematically in Fig. 1. The simplified 4-grain microstructure is shown in Fig. 1(a) and the corresponding binary tree is shown in Fig. 1(b). In this example, grains A and B, and grains C and D interact across two planar grain boundaries. The interaction between grains A and C, or B and D is however, not modeled directly. Instead, grains A and B are collected together to form a sub-aggregate, named 1. Similarly grains C and D form the sub-aggregate 2. 1 and 2 then interact across an approximately planar facet (dashed line) to form a 4-grain sub-aggregate R. The binary tree, shown in Fig. 1 (b), represents the interactions.

The present binary tree representation was obtained by discretizing the experimentally measured X-ray texture into a set of 2^{12}= 4096 orientations of equal volume fraction. These orientations were assigned to the leaves of a balanced binary tree of height 13, each of which now represents a grain, such as A, B, C or D in Fig. 1. It was ensured that sufficiently many grains were included in the model by performing one simulation with twice as many grains, and verifying that the predicted stress-strain response and twin volume fractions were altered insignificantly. The neighbors of a grain are not known from the X-ray texture. They can be obtained from EBSD scans. However, in previous work [22] we have observed that whereas the deformation of a specific grain does depend on its neighboring grains within the model, statistical properties computed over the model polycrystalline aggregate do not. It is of interest presently to obtain statistical properties such as the polycrystalline mechanical response, and twin volume fraction. Therefore, the model texture was not initialized with information from EBSD scans. Instead, pairs of grains drawn at random from the discretized X-ray texture were

formed at random, and required to interact across a planar grain boundary facet. The orientations of the planar facets are themselves drawn at random from a uniform distribution [22].

In the binary-tree based model [26], field variables such as stresses $\sigma_{[k]}$ and strain-rates $\dot{\varepsilon}_{[k]}$ of node $[k]$ are defined as volume-fraction weighted averages of the corresponding fields over the children:

$$\sigma_{[k]} = \frac{\left\{w_{[l(k)]}\sigma_{[l(k)]} + w_{[r(k)]}\sigma_{[r(k)]}\right\}}{w_{[k]}}, \tag{2}$$

and

$$\dot{\varepsilon}_{[k]} = \frac{\left\{w_{[l(k)]}\dot{\varepsilon}_{[l(k)]} + w_{[r(k)]}\dot{\varepsilon}_{[r(k)]}\right\}}{w_{[k]}}. \tag{3}$$

Also, the interface between the sub-aggregates represented by sibling nodes in the binary tree is assumed to be planar. Let the planar interface between the sibling nodes $[l(k)]$ and $[r(k)]$ be oriented normal to $\nu_{[k]}$. Continuity of traction and velocity between sibling nodes across this planar interface requires that

$$\left\{\sigma_{[l(k)]} - \sigma_{[r(k)]}\right\} \cdot \nu_{[k]} = 0, \tag{4}$$

and

$$t_{[k]} \cdot \left\{\dot{\varepsilon}_{[l(k)]} - \dot{\varepsilon}_{[r(k)]}\right\} \cdot t_{[k]} = 0, \forall\, t_{[k]} \perp \nu_{[k]}. \tag{5}$$

In low-symmetry materials, accommodative plastic strains at grain boundaries differ significantly from that in the grain bulk [34]. Staroselsky and Anand [35] modeled the deformation of the grain boundary region using rate-dependent isotropic plasticity, while treating the deformation of the grain bulk using a rate-independent framework. Following their approach, each present grain is conceptually divided into a near grain boundary region, and a grain bulk region. Let their volume fractions be f_{gb}, and $1 - f_{\mathrm{gb}}$, respectively. Approximately isotropic rate-independent plasticity in the grain boundary region is realized by the following construction: An fcc unit cell is superposed on the unit cell of the hcp crystal such that the fcc $[100]$ and $[001]$ directions coincide with the hcp a, and c-axes, respectively. Miller indices of the hcp slip systems that coincide with the 24 fcc $\{111\}\langle 110\rangle$ slip systems are obtained. These slip systems, denoted S_1 in the sequel, are assumed to accommodate the grain boundary deformation. Plastic

deformation of the grain bulk, on the other hand, is accommodated by the typical hcp prismatic, pyramidal and extension twinning systems [36]. This latter set of slip and twinning systems operating in the grain bulk is denoted S_2.

Let $\dot{\gamma}^s_{[k]}$ denote the slip-rate in the s-th slip or twin system and let $m^s_{[g]}$ denote the Schmid tensor of slip or twin system s. Then, the accommodation of the imposed strain-rate on grain k may be expressed as

$$\dot{\varepsilon}_{[k]} = f_{\text{gb}} \sum_{s \in S_1} \dot{\gamma}^s_{[k]}\, m^s_{[k]} + \left(1 - f_{\text{gb}}\right) \sum_{s \in S_2} \dot{\gamma}^s_{[k]}\, m^s_{[k]}\,. \tag{6}$$

The two terms in Eq. (6) correspond to contributions from the grain boundary and from the grain bulk regions, respectively. Schmid's law [37] is assumed to govern the activation of all slip and twinning systems. If the critical resolved shear stress of slip system or twinning system s in grain k is denoted $\tau^s_{[k]}$, the resolved shear stress on this system is given by $\sigma_{[k]}\colon m^s_{[k]}$, and the slip rate is given by

$$\dot{\gamma}^s_{[k]} \begin{cases} = 0, \text{ if } \sigma_{[k]}\colon m^s_{[k]} < \tau^s_{[k]} \\ \geq 0, \text{ if } \sigma_{[k]}\colon m^s_{[k]} = \tau^s_{[k]} \\ \dot{\gamma}^s_{[k]} \text{undefined, otherwise.} \end{cases} \tag{7}$$

In this scheme, the two senses of slip (positive and negative Burgers vectors) of a slip system are regarded as two different slip systems. Twinning systems have only one sense of shear. Note also that the grain stress, $\sigma_{[k]}$, is assumed uniform in both the grain boundary and grain bulk regions in this treatment.

The first term in Eq. (6), representing grain boundary accommodation, has been introduced to bound the macroscopic stresses; its omission is found to result in unrealistically high stress values. This is exactly as observed by Staroselsky and Anand [35] in their crystal plasticity based finite element model. The commonality between the present model and that of Staroselsky and Anand [35] is that both models explicitly account for intergranular interactions across grain boundaries. On the other hand, the viscoplastic self-consistent model of Lebensohn and Tomé [10], which has been extensively applied to model the plastic deformation of hcp materials, requires no such accounting for grain boundary accommodation. This is because a typical grain in the self-consistent model does not directly interact with other grains. It interacts with a

homogeneous effective medium representing all the grains. The grain boundary accommodation in this case is subsumed within the latter interaction. In other words, the typical grain in the self-consistent model approximately corresponds to the region of the grain designated as the grain bulk in the present treatment.

Although inhomogeneous distribution of slip-rates, $\dot{\gamma}^{s}_{[k]}$, has been assumed in Eq. (6), it is mathematically permissible, and convenient in the present rate-independent framework to 'smear' the slip-rates over the entire domain: Let

$$\dot{\gamma}^{s,*}_{[k]} = \begin{cases} f_{\mathrm{gb}}\,\dot{\gamma}^{s}_{[k]}, \text{ if } s \in S_1, \\ (1 - f_{\mathrm{gb}})\dot{\gamma}^{s}_{[k]}, \text{ if s} \in S_2. \end{cases} \tag{8}$$

Here, $\dot{\gamma}^{s,*}_{[k]}$ represents the smeared slip-rates, homogenized over the domain of a grain. It follows from Eqs. (6) and (8) that

$$\dot{\varepsilon}_{[k]} = \sum_{s \in S_1 \cup S_2} \dot{\gamma}^{s,*}_{[k]}\, m^{s}_{[k]}\,. \tag{9}$$

It can be easily seen that within the framework of rate-independent plasticity, the plastic power associated with $\dot{\gamma}^{s,*}_{[k]}$ distributed over the entire domain equals that associated with the inhomogeneous slip-rates leading up to Eq. (6). It is clear from Eq. (9) that f_{gb} need not be fixed if only the overall deformation of grains is of interest.

Slip and twinning systems are assumed to harden following the extended Voce law [11,38]. Suppressing the subscript k for clarity, the hardening of slip system s follows:

$$\tau^{s} = \tau^{s}_{0} + (\tau^{s}_{1} + \theta^{s}_{1}\Gamma)\left\{1 - \exp\left(-\frac{\theta^{s}_{0}\Gamma}{\tau^{s}_{1}}\right)\right\}, \tag{10}$$

where, Γ denotes the total accumulated slip in the grain, and $\tau^{s}_{0}(T,\dot{\epsilon})$, $\tau^{s}_{1}(T,\dot{\epsilon})$, $\theta^{s}_{0}(T,\dot{\epsilon})$, and $\theta^{s}_{1}(T,\dot{\epsilon})$ denote temperature (T), and strain-rate ($\dot{\epsilon}$) dependent material parameters associated with slip system s. These material parameters are assumed independent of the state of deformation, Γ. Interaction between the various slip and twinning modes is captured using the self (h_{ss}) and latent ($h_{ss'}$) hardening coefficients [39] following

$$\dot{\tau}^s = \frac{d\hat{\tau}^s}{d\Gamma} \sum_{s'} h_{ss'} \dot{\gamma}^{s'}. \tag{11}$$

Here, τ_s denotes the critical resolved shear stress (CRSS) of slip system s, $\dot{\tau_s}$ denotes the rate of change of the CRSS of slip system s, and $\dot{\gamma}^s$ denotes the slip rate in system s.

Activation of twinning systems and accommodation of shear by their activation entails a transformation of the lattice orientation of the grain matrix [37,40]. Following the methodology proposed by Van Houtte [7], the volume fraction f_t of twin variant t depends on the accumulated shear γ_t in twinning system t and its characteristic twinning shear, Γ_t as:

$$f_t = \gamma_t / \Gamma_t. \tag{12}$$

The growth of twins is accounted for simply by the increase of f_t in the model. Twinned volumes are not explicitly expressed as new leaf nodes in the binary tree based model. Thus, slip or re-twinning within the twinned volume is not modeled.

4. Results

Crystallographic textures developed after a tensile strain of 0.25 are summarized in Fig. 2. The deformation textures had two fibres: (0001) and $\langle 1\bar{1}00 \rangle$. Both the specimens, RD and TD, had the basal (0001) fiber. Partial $\langle 1\bar{1}00 \rangle$ fiber existed primarily in the RD specimen. However, the crystallographic texture development did not depend on the working temperature. Textures differed with sample orientation (RD or TD), but appeared independent of the working temperature. Variations in the mechanical response with temperature cannot therefore be attributed to variations in the texture evolution.

The microstructures associated with tensile deformations are shown in Fig. 3. Two types of microstructural observation were made. Direct or ex-situ, where the same grains were studied with progressive tensile deformation. Such observations were, however, more painstaking and covered a temperature range of 123 K to 298 K. Indirect or statistical measurements were taken for specimens deformed at 623 K. Surface oxidation, even under inert atmosphere, makes direct observations on the specimen surface an impossible task at this higher temperature. Direct (Fig. 3(a)) and indirect (Fig. 3(b)) observations showed deformation twinning. As shown in Fig. 3(b),

deformation twinning was more in TD specimen, and twin morphology varied significantly with working temperature.

Deformation twinning is quantified in Fig. 4. Two types of extension twins were noted: $\{10\bar{1}2\}\langle\bar{1}011\rangle$ and $\{11\bar{2}1\}\langle\bar{1}\bar{1}26\rangle$. The characteristic shear strains, Γ_t in Eq. (12), for these two types of twins is 0.169, and 0.628, respectively [37,40]. The area fraction of both types of twinned regions corresponding to the four working temperatures, and two loading directions, is shown in Fig. 4(a) after 0.25 tensile strain. Consistent with observations in the literature, the twin area fraction was found increase with decreasing temperature. In the RD specimen, the area fraction at the lowest testing temperature was sparse: the twinning area fraction was less than 2% after 25% strain. In the TD specimens, however, twinning is not sparse at the two lowest testing temperatures: twinning area fractions of about 10% and 5% were measured. Even so, the twin area fractions measured presently are markedly less than that in specimen oriented favourably for tensile twinning. Kaschner et al. [12] measured twin volume fraction as high as 59% in a specimen compressed to 28% strain along an in-plane direction at 78 K.

Fig. 4(b) shows the number fraction of twinned regions at the same strain level. $\{10\bar{1}2\}\langle\bar{1}011\rangle$ twins were observed at all working temperatures. $\{11\bar{2}1\}\langle\bar{1}\bar{1}26\rangle$ twins, on the other hand, were observed only at low temperatures. The estimated ratios of these two twin types are shown in Fig. 4(c) for the TD specimen, for which twinning was more pronounced. An important difference in the morphology of the twinned grains was also observed. As shown in Fig. 4(d), the estimated width of the twin grains increased with working temperature. It needs to be noted that data of Fig. 4 was obtained from manual identification of the twins, twin parent and product grains. An automated analysis, based on twin orientation relationship, often has problems of deformation induced misorientation developments [22,41,42] and cannot yield accurate data on deformation twin characterization.

Though deformation twinning did depend on the crystallographic orientation (Fig. 5), as revealed by direct observations this 'selection' did not seem to vary with the working temperature. The extent of twinning was more at the lower temperatures (Figs. 4(a) and 4(b)), but the orientations of twin-parent and non-twinned grains (Fig. 5) did not change. In-grain misorientation developments (kernel average misorientation or KAM: Fig. 6(a) and grain average misorientation or GAM: Fig. 6(b)) did depend on the tensile strain, but appeared

independent of the working temperature. KAM is defined as average misorientation between each measurement point and its immediate neighbours (six – for the hexagonal grid used), excluding misorientations below 5°. On the other hand, GAM represents average misorientation between neighbouring measurement points inside an EBSD grain defined by the presence of a continuous boundary of ≥ 5° misorientation. Figs. 6(a) and 6(b) collate the direct observations. Though the deformation twinning reduced by nearly one order of magnitude (Fig. 4(a)) over the studied temperature range, the misorientations remained within a very narrow band. However, specimens with lower twinning (RD) appeared to have slightly higher in-grain misorientations (KAM: Fig. 6(c) and GAM: Fig. 6(d)).

From the direct observations, and corresponding high resolution EBSD data, the mesoscopic shear strains can be estimated. This procedure is explained elsewhere [34]. An earlier study [22], based on the same procedure showed that the grains undergoing deformation twinning had higher near boundary mesoscopic shear (NBMS) strains. It was stipulated [22] that high NBMS stimulate deformation twinning. As shown in Fig. 7(a), the NBMS were estimated in the present specimens as well. It is clear (see Fig. 7(b)) that the twin-parent grains had higher NBMS: estimated as both grain average and maximum shear strains. In other words, the observation on the possible selection of grains for twin nucleation through higher near boundary shear (and correspondingly higher dislocation activities) appear to be valid over the entire range of working temperatures. The observation of significant NBMS justifies the separate accounting for near grain boundary accommodation modes in Eq. (6).

The true stress (σ)-true plastic strain (ε) plots for the four testing temperatures are shown in Fig. 8(a). A marked influence of working temperature is evident. The testing direction, RD or TD, has a smaller influence. The present flow stress curves lack inflection points, i.e., they are not S-shaped. This contrasts with the flow stress curves reported in the literature for zirconium exhibiting intense deformation twining [12,20]. The work-hardening rate derived from Fig. 8(a) is plotted in Fig. 8(b) as $\frac{d\sigma}{d\epsilon}$ versus σ. It is clear that TD specimens had higher work hardening, especially at the lower working temperatures. Also shown in Figs. 8(c) and 8(d) are the ratios of the measured flow stresses at various temperatures, with that corresponding to a reference temperature, arbitrarily chosen as 298 K. It is clear from Fig. 8(c) that beyond a small initial plastic strain, say 0.05, the ratio becomes nearly constant in all RD specimen. Amongst the TD

specimens, shown in Fig. 8(d), the flow stress ratio becomes nearly constant for the 623 K data. Visible deviations from constancy of the flow stress ratio are observed in the case of TD specimens tested at 123 K and 203 K, in Fig. 8(d). Quantitatively, the root mean squared (r.m.s.) deviation for the flow stress ratios at 123 K and 203 K are 0.02 and 0.01, respectively. The corresponding r.m.s. deviation at 623 K is an order of magnitude less, 0.001. All r.m.s. values are computed using flow stress ratios for plastic strains greater than 0.05. Significantly, the lowest temperatures, 123 K and 203 K also correspond to the largest twin area fractions, about 10% and 5% in (Fig. 4a).

The measured tensile Cauchy (true) stresses at room temperature (298 K) are plotted in Fig. 9 (a) and (b) against plastic strain, corresponding to RD and TD tension, respectively. Also shown are predictions obtained from the binary tree model based simulations, described previously in Sec. 3**.** The Voce hardening parameters used to obtain the predicted lines are given in Table 2. The assumed slip and twin modes are also listed in this table. The same set of parameters yields the predictions for uniaxial tension along both RD and TD. The chosen parameters indicate that prismatic slip is the softest deformation mode. Other deformation modes are much harder than prismatic slip. The softest mode amongst these hard modes is grain boundary accommodation. Pyramidal slip is the hardest slip mode. Both $\{10\bar{1}2\}\langle\bar{1}011\rangle$ and $\{11\bar{2}1\}\langle\bar{1}\bar{1}26\rangle$ extension twinning are assigned negligible hardening. The former is however, much softer than the latter, as is evident from Table 2. Also, according to the chosen latent hardening parameters, $\{10\bar{1}2\}\langle\bar{1}011\rangle$ extension twinning strongly latent hardens other slip and twin systems; the mutual interaction of other slip and twinning systems is much weaker. These trends are consistent with those reported in the literature [11,12] for zirconium.

The material parameters $\tau_0^s(T,\dot{\epsilon})$, $\tau_1^s(T,\dot{\epsilon})$, $\theta_0^s(T,\dot{\epsilon})$, and $\theta_1^s(T,\dot{\epsilon})$ required to fit the experimental stress-strain curves for the other temperatures, viz., 123 K, 203 K and 623 K at constant strain-rate $\dot{\epsilon} = 2\times10^{-5}\ /s$ were also determined. These were found to be related to the reference temperature (298 K) parameters in a surprisingly simple way. It was possible to fit the experimentally measured stress-strain curves at 123 K, 203 K and 623 K, shown in Figs. 9(a), and (b), by merely scaling all the reference temperature material parameters $\tau_0^s(298\,K,\dot{\epsilon})$, $\tau_1^s(298\,K,\dot{\epsilon})$, $\theta_0^s(298\,K,\dot{\epsilon})$, and $\theta_1^s(298\,K,\dot{\epsilon})$ by two temperature dependent factors. One factor, $\kappa(T)$ scales the parameters corresponding to the slip and twinning systems potentially activating

within the grain bulk, while the other, $\kappa_{\mathrm{gb}}(T)$, scales the grain boundary constants. Both functions only depend on temperature and not on the current hardening state. Factors $\kappa(T)$ and $\kappa_{\mathrm{gb}}(T)$ for the present set of temperatures are tabulated in Table 3. The latent hardening parameters are assumed temperature independent. Thus, the extended Voce hardening law, Eq. (10), can be written in the form

$$\tau = \kappa(T, \dot{\epsilon}) \left[\hat{\tau}_0 + \left(\hat{\tau}_1 + \hat{\theta}_1 \Gamma \right) \left\{ 1 - \exp\left(-\frac{\Gamma \hat{\theta}_0}{\hat{\tau}_1} \right) \right\} \right] \tag{14}$$

for the grain bulk deformation modes. Here, $\hat{\tau}_0$, $\hat{\tau}_1$, $\hat{\theta}_0$, and $\hat{\theta}_1$ denote temperature, strain-rate, and deformation state-independent material constants. It must be noticed that such a multiplicative decomposition is unlikely in fcc, or bcc (body centered cubic) materials, wherein the temperature sensitivities of the yield point and work hardening are known to follow widely dissimilar trends [43].

The twin volume fraction predicted by the binary tree based model (Fig. 9(c)) after tensile deformation shows good agreement with the experimental measurements. The grain boundary accommodation modes, introduced following Staroselsky and Anand [35], are crucially important to bring about this agreement. Disallowing grain boundary accommodation will result in much larger twin volume fraction predictions, exactly as observed by Staroselsky and Anand [35].

5. Discussion

Specimens cut along the rolling and transverse directions of a strongly textured Zircaloy-4 sheet were subjected to uniaxial tensile deformation up to about 25% strain at four temperatures: 123 K, 203 K, 298 K, and 623 K. Stress-strain curves, final texture, and final microstructure were observed. Texture evolution is mostly independent of temperature in the present range. Quantitative descriptors of the final microstructure were obtained. In particular, twin area fraction after deformation was manually measured. Extension twins of two types: $\{10\bar{1}2\}\langle\bar{1}011\rangle$ and $\{11\bar{2}1\}\langle\bar{1}\bar{1}26\rangle$ were observed in the present specimens, with the latter having an appreciable volume fraction only at the lowest test temperature, 123 K. The binary tree based

polycrystal plasticity model [26] was used to simulate the observed tensile deformation. The model could capture both stress evolution with strain, and the final twin volume fraction accurately, provided grain boundary accommodation is explicitly modeled.

5.1 Exponential scaling

According to Eq. (14), slip and twin system hardness permits multiplicative decomposition into temperature/strain-rate and accumulated strain dependent parts. The temperature and strain-rate dependence is contained in $\kappa(T, \dot{\epsilon})$, while the strain dependence is contained in the extended Voce factor within square brackets in Eq. (14). As shown by the semi-logarithmic plot in Fig. 10, the temperature variation of modulus corrected $\kappa(T, \dot{\epsilon})$ at constant strain-rate $\dot{\epsilon} = 2\times10^{-5}\ /s$ is well-approximated by

$$\kappa(T, \dot{\epsilon} = 2\times10^{-5}\ /s)\,\frac{\mu_0}{\mu(T)} = \kappa_0 \exp\left(-\frac{T}{T_0}\right), \tag{15}$$

with the parameters $\kappa_0 = 2.2$, and $T_0 = 400\ K$. Here, μ denotes the temperature-dependent shear modulus, which, following Beyerlein and Tomé [13] is assumed to obey $\mu(T) = 40.06$ GPa $- 0.022\,T$ GPa/K. μ_0 denotes the shear modulus at zero temperature. The exponential scaling of Eq. (15) was proposed by Kocks [28] for the saturation stress normalized by the shear modulus, and by Haasen [44] for the critical resolved shear stress at the onset of stage III in nickel single crystals. It is also seen from Fig. 10 that $\kappa_{\mathrm{gb}}(T)$ associated with the grain boundary modes does not scale exponentially following Eq. (15). This suggests that the mechanisms underlying grain boundary accommodation are different from those accommodating the deformation of the grain bulk.

5.2 Kocks-Mecking phenomenological scaling

In single-phase fcc materials accommodating plastic deformation exclusively by slip, Kocks et al. [4,45] proposed the following phenomenological scaling for the saturation stress, σ_v, at temperature T and strain-rate $\dot{\epsilon}$:

$$\frac{\sigma_v}{\mu}\frac{\mu_0}{\sigma_{v_0}} = \left[1 - \left(\frac{kT}{F_0}\ln\frac{\dot{\epsilon}_0}{\dot{\epsilon}}\right)^{1/2}\right]^2 . \tag{16}$$

Here, σ_{v_0} denotes the saturation stress values at zero temperature, respectively, F_0 is the activation energy at zero stress, k is the Boltzmann constant and $\dot{\epsilon}_0$ is a reference strain-rate, taken to be $10^7/s$, following Beyerlein and Tomé [13]. In the notation of the extended Voce law of Eq. (10), σ_v of Eq. (16) corresponds to $\tau_0^s + \tau_1^s$.

The multiplicative decomposition of Eq. (14), and Eq. (16) motivate consideration of the scaling:

$$\frac{\kappa(T,\dot{\epsilon})}{\mu}\frac{\mu_0}{\kappa_0} = \left[1 - \left(\frac{kT}{F_0}\ln\frac{\dot{\epsilon}_0}{\dot{\epsilon}}\right)^{1/2}\right]^2 . \tag{17}$$

Assuming $\kappa_0 = 3.2$, and $\frac{k\ln(\dot{\epsilon}_0/\dot{\epsilon})}{F_0} = 1/(2050\ K)$, Fig. 11 plots the variation of the left and right sides of Eq. (17) with temperature. Good comparison is obtained at all temperatures within the studied range. This suggests that the phenomenological scaling evolved for fcc materials, given by Eq. (16), is also applicable for hcp materials. However, Fig. 11 also shows that Eq. (11) does not apply to the grain boundary modes, $\kappa_{\mathrm{gb}}(T)$. As in Sec. 5.1, this suggests that the some of the mechanisms accommodating grain boundary deformation may be different from that of the grain bulk. It is speculatively suggested that twin nucleation may be one such mechanism.

A limitation of the comparison shown in Fig. 11 is that Eq. (17) has been validated for varying temperatures, but not for varying strain-rates. Temperature and strain-rate feature in Eq. (17) through the factor $kT\ln(\dot{\epsilon}_0/\dot{\epsilon})$. This factor arises by inverting the Arrhenius law of thermal activation [45]

$$\dot{\varepsilon} = \dot{\epsilon}_0 \exp(-\Delta G\ (\sigma)/kT), \tag{18}$$

where, $\dot{\epsilon}_0$ is a constant, and $\Delta G\ (\sigma)$ is the stress-dependent activation free energy. In only validating Eq. (17) against temperature change tests, Eq. (18) has been tacitly assumed to hold for the present material and loading conditions.

In nominally the same material (Zircaloy-4) and loading conditions (in plane tension) as the present study, Derep et al. [46] evaluated the enthalpy and free energy of activation of pinned dislocations. They employed the thermodynamic formulae derived previously by Schoeck [47]. Shoeck's formulae assume the validity of Eq. (18), and require flow stress data from both temperature and strain-rate change tests, to evaluate. Shoeck's formulation yields the enthalpy and free energy through a pair of complementary formulae. Coincidence of their results confirms the validity of Eq. (18). Derep et al. [46], in their Fig. 5, show that coincidence is obtained up to about $T = 400$ K. Taking this value of T, and taking $\dot{\epsilon} = 3.3\times10^{-5}$/s, which corresponds to the lowest strain-rate employed in the tests of Derep et al. [46], a threshold value of $kT\ln(\dot{\epsilon}_0/\dot{\epsilon}) \approx 0.91$ eV is obtained. This defines the upper bound of the regime in which the law of thermal activation, Eq. (18) holds. Three of the four temperatures studied presently (123 K, 203K, 298 K), at the present strain-rate of $\dot{\epsilon} = 2\times10^{-5}$/s fall within the regime of validity of Eq. (18). For $kT\ln(\dot{\epsilon}_0/\dot{\epsilon}) > 0.91$ eV, it is expected that Eq. (18) will not hold, and the scaling given by Eq. (17) will deviate from experimental measurements.

The fourth test temperature, 623 K, falls near the beginning of an athermal regime, wherein $\Delta G\ (\sigma)$ is undefined [46,48–53]. The stress becomes insensitive to temperature in this regime, and Eq. (18) no longer applies. The scaling of Eq. (17) should not be expected to apply at this temperature. Even so, it is seen from Fig. 11 that the deviation between the left and right sides of Eq. (18) is quite small even at 623 K.

Assuming dislocation glide as the only mechanism of plastic deformation, the aforementioned works [46,48–53] have proposed rate-controlling dislocation processes over regimes of continuity of $\Delta G\ (\sigma)$. There is ongoing debate over the rate-controlling mechanisms, and direct in situ observations, made in recent years may offer a satisfactory resolution in the near future [54]. But the basis of Eqs. (15) and (17) is strictly phenomenological. Their empirical validity, shown in Figs. 10 and 11, is therefore secure even without a detailed understanding of the dislocation mechanisms.

In fcc materials, it is well-known [4] that the initial yield stress is relatively insensitive to temperature, but that the work hardening slope is much more temperature sensitive. In bcc materials, the positions are reversed. The initial yield point is typically more temperature sensitive than the work hardening. It is only in the intermediate case of hcp materials [43], that

temperature sensitivity of both initial yield and work-hardening parameters may be comparable. In the present Zircaloy-4, it turns out that both initial yield and work hardening manifest essentially identical temperature dependence. For this reason, although the fcc scaling, Eq. (16), was proposed by Kocks et al. [4,45] only for the saturation stress, the scaling given by Eq. (17) applies to all aspects of the hardening curve, including initial yield τ_0^s, and stage IV hardening slope, θ_1^s. The same is also true for the exponential scaling of Eq. (15).

5.3 Effect of deformation twinning

Eqs. (14), (15) and (17) are contingent upon the twinning volume fraction being small enough to not significantly affect material work hardening. A breakdown of these simple relationships with increasing twinning is already suggested by the present data. Fig. 4 shows that the largest twin fractions of about 10% are obtained in TD tension at 123 K and 203 K. It is the flow stress ratios for precisely these two cases that show the greatest deviations from constancy in Fig. 8(d), as discussed previously in Sec. 4. This implies that the multiplicative decomposition in Eq. (14) begins to breakdown in these cases, although not yet sufficiently to disrupt reasonable agreement between predicted and experimental stress-strain curves in Figs. 9(a) and (b).

For larger twinning volume fractions, the simple temperature dependence of Eq. (14) is known to fail. In their experiments, Tomé et al. [11] and Kaschner et al. [12] loaded their specimen along directions that were favorable for deformation twinning. The Voce hardening parameters given by Tomé et al. [11] and Kaschner et al. [12] at 76 K and 293 K do not satisfy the simple relationship given by Eq. (14). This suggests that Eqs. (14), and (17) breakdown whenever complex slip-twin interactions become important in the work hardening process.

6. Conclusions

Uniaxial tensile tests have been performed on strongly textured polycrystalline Zircaloy-4 samples along directions that are nominally unfavorable for extensive twinning at temperatures of 123 K, 203 K, 298 K and 623 K. The tests establish clear trends in the deformation twinning and work hardening behavior with temperature. The phenomenological hardening law of slip and twinning systems in these systems admits of a multiplicative decomposition into temperature and

strain dependent parts. Furthermore, the former admits of phenomenological scalings proposed by Kocks, Haasen, Mecking and co-workers for single-phase non-twinning fcc materials. These conclusions breakdown if slip-twin interactions are important in the work-hardening process.

Acknowledgments

This research was supported by the Board of Research in Nuclear Science (BRNS) and by the National Facility of Texture and OIM, a DST-IRPHA facility at IIT Bombay, Mumbai, India. We also thank the reviewer for important criticisms that led to improvement in the modeling effort.

References

[1] N.F. Mott F.R.S., CXVII. A theory of work-hardening of metal crystals, London, Edinburgh, Dublin Philos. Mag. J. Sci. Ser. 7. 43 (1952) 1151–1178. doi:10.1080/14786441108521024.

[2] U.F. Kocks, A statistical theory of flow stress and work-hardening, Philos. Mag. 13 (1966) 541–566. doi:10.1080/14786436608212647.

[3] Y. Estrin, H. Mecking, A unified phenomenological description of work hardening and creep based on one-parameter models, Acta Metall. 32 (1984) 57–70. doi:10.1016/0001-6160(84)90202-5.

[4] U.F. Kocks, H. Mecking, Physics and phenomenology of strain hardening: the FCC case, Prog. Mater. Sci. 48 (2003) 171–273. doi:10.1016/S0079-6425(02)00003-8.

[5] A. Seeger, G. Schöck, The splitting of dislocations in metals with close-packed lattices, Acta Metall. 1 (1953) 519–530. doi:10.1016/0001-6160(53)90082-0.

[6] U.F. Kocks, D.G. Westlake, The Importance of Twinning for the Ductility of CPH Polycrystals, Trans. AIME. 239 (1967) 1107–1109.

[7] P. Van Houtte, Simulation of the rolling and shear texture of brass by the Taylor theory adapted for mechanical twinning, Acta Metall. 26 (1978) 591–604. doi:10.1016/0001-6160(78)90111-6.

[8] S.R. Kalidindi, Modeling anisotropic strain hardening and deformation textures in low stacking fault energy fcc metals, Int. J. Plast. 17 (2001) 837–860. doi:10.1016/S0749-6419(00)00071-1.

[9] T. Leffers, R.K. Ray, The brass-type texture and its deviation from the copper-type texture, Prog. Mater. Sci. 54 (2009) 351–396. doi:10.1016/j.pmatsci.2008.09.002.

[10] R.A. Lebensohn, C.N. Tomé, A self-consistent anisotropic approach for the simulation of plastic deformation and texture development of polycrystals: application to zirconium alloys, Acta Met. Mater. 41 (1993) 2611–2624.

[11] C.N. Tomé, P.J. Maudlin, R.A. Lebensohn, G.C. Kaschner, Mechanical response of zirconium—I. Derivation of a polycrystal constitutive law and finite element analysis,

Acta Mater. 49 (2001) 3085–3096.

[12] G.C. Kaschner, C.N. Tomé, I.J. Beyerlein, S.C. Vogel, D.W. Brown, R.J. McCabe, Role of twinning in the hardening response of zirconium during temperature reloads, Acta Mater. 54 (2006) 2887–2896. doi:10.1016/j.actamat.2006.02.036.

[13] I.J. Beyerlein, C.N. Tomé, A dislocation-based constitutive law for pure Zr including temperature effects, Int. J. Plast. 24 (2008) 867–895. doi:10.1016/j.ijplas.2007.07.017.

[14] J.J. Gilman, Toward physically-based rate laws for dislocations, Mater. Sci. Eng. A. 322 (2002) 126–131. doi:10.1016/S0921-5093(01)01125-X.

[15] H. Qiao, P.D. Wu, H. Wang, M.A. Gharghouri, M.R. Daymond, Evaluation of elastic–viscoplastic self-consistent polycrystal plasticity models for zirconium alloys, Int. J. Solids Struct. 71 (2015) 308–322. doi:10.1016/j.ijsolstr.2015.07.004.

[16] H. Abdolvand, M.R. Daymond, C. Mareau, Incorporation of twinning into a crystal plasticity finite element model: Evolution of lattice strains and texture in Zircaloy-2, Int. J. Plast. 27 (2011) 1721–1738. doi:10.1016/j.ijplas.2011.04.005.

[17] G. Proust, C.N. Tomé, G.C. Kaschner, Modeling texture, twinning and hardening evolution during deformation of hexagonal materials, Acta Mater. 55 (2007) 2137–2148. doi:10.1016/j.actamat.2006.11.017.

[18] C.C. Aydıner, J.V. Bernier, B. Clausen, U. Lienert, C.N. Tomé, D.W. Brown, Evolution of stress in individual grains and twins in a magnesium alloy aggregate, Phys. Rev. B. 80 (2009) 024113(1-6). doi:10.1103/PhysRevB.80.024113.

[19] R.J. McCabe, G. Proust, E.K. Cerreta, A. Misra, Quantitative analysis of deformation twinning in zirconium, Int. J. Plast. 25 (2009) 454–472. doi:10.1016/j.ijplas.2008.03.010.

[20] R.J. McCabe, E.K. Cerreta, A. Misra, G.C. Kaschner, C.N. Tomé, Effects of texture, temperature and strain on the deformation modes of zirconium, Philos. Mag. 86 (2006) 3595–3611. doi:10.1080/14786430600684500.

[21] H. Li, G. Sun, W. Woo, J. Gong, B. Chen, Y. Wang, Y.Q. Fu, L. Xie, S. Peng, Tensile deformation behaviors of Zircaloy-4 alloy at ambient and elevated temperatures: In situ neutron diffraction and simulation study, J. Nucl. Mater. 446 (2014) 134–141. doi:10.1016/j.jnucmat.2013.12.006.

[22] J. Singh, S. Mahesh, G. Kumar, P. Pant, D. Srivastava, G.K. Dey, N. Saibaba, I. Samajdar, Deformation Twinning in Zirconium: Direct Experimental Observations and Polycrystal Plasticity Predictions, Metall. Mater. Trans. A. 46 (2015) 5058–5071. doi:10.1007/s11661-015-3085-z.

[23] B. Luan, S. Gao, L. Chai, X. Li, A. Chapuis, Q. Liu, Compression deformation behavior of Zr–1Sn–0.3Nb alloy with different initial orientations at 650°C, Mater. Des. 52 (2013) 1065–1070. doi:10.1016/j.matdes.2013.06.069.

[24] H.A. Padilla II, C.D. Smith, J. Lambros, A.J. Beaudoin, I.M. Robertson, Effects of deformation twinning on energy dissipation in high rate deformed zirconium, Metall. Mater. Trans. A. 38 A (2007) 2916–2927. doi:10.1007/s11661-007-9365-5.

[25] J.P. Escobedo, E.K. Cerreta, C.P. Trujillo, D.T. Martinez, R.A. Lebensohn, V.A. Webster, G.T. Gray III, Influence of texture and test velocity on the dynamic, high-strain, tensile behavior of zirconium, Acta Mater. 60 (2012) 4379–4392. doi:10.1016/j.actamat.2012.05.001.

[26] S. Mahesh, A binary-tree based model for rate-independent polycrystals, Int. J. Plast. 26 (2010) 42–64.

[27] J. Singh, S. Mahesh, G. Kumar, P. Pant, D. Srivastava, G.K. Dey, N. Saibaba, I. Samajdar, Texture Development and Plastic Deformation in a Pilgered Zircaloy-4 Tube, Metall. Mater. Trans. A. 46 (2015) 1927–1947.

[28] U.F. Kocks, Laws for work-hardening and low-temperature creep, J. Eng. Mater. Technol. 98 (1976) 76–85.

[29] K.V.M. Krishna, A. Sain, I. Samajdar, G. Dey, D. Srivastava, S. Neogy, R. Tewari, S. Banerjee, Resistance to hydride formation in zirconium: An emerging possibility, Acta Mater. 54 (2006) 4665–4675.

[30] M.M. Nowell, S.I. Wright, Orientation effects on indexing of electron backscatter diffraction patterns, Ultramicroscopy. 103 (2005) 41–58. doi:10.1016/j.ultramic.2004.11.012.

[31] B.D. Cullity, S.R. Stock, Elements of X-ray Diffraction, 3rd Edition, Prentice Hall, New Jersey, 2001.

[32] D. Raabe, K. Lücke, Investigation of the ADC method for direct ODF approximation by means of standard functions, Phys. Status Solidi (b). 180 (1993) 59–65.

[33] T.H. Cormen, C.E. Leiserson, R.L. Rivest, C. Stein, Introduction to Algorithms, 3rd Editio, MIT press, Cambridge, 2009. doi:10.1111/dme.12379.

[34] N. Keskar, S. Mukherjee, K.V.M. Krishna, D. Srivastava, G.K. Dey, P. Pant, R.D. Doherty, I. Samajdar, Quantifying the mesoscopic shear strains in plane strain compressed polycrystalline zirconium, Acta Mater. 69 (2014) 265–274. doi:10.1016/j.actamat.2014.01.023.

[35] A. Staroselsky, L. Anand, A constitutive model for hcp materials deforming by slip and twinning: application to magnesium alloy AZ31B, Int. J. Plast. 19 (2003) 1843–1864.

[36] E. Tenckhoff, Deformation mechanisms, texture, and anisotropy in zirconium and zircaloy, ASTM Spec. Tech. Publ. 966. (1988) 1–77.

[37] U.F. Kocks, C.N. Tomé, H.-R. Wenk, Texture and Anisotropy, Cambridge University Press, Cambridge, U.K., 1998.

[38] C. Tome, G.R. Canova, U.F. Kocks, N. Christodoulou, J.J. Jonas, The relation between macroscopic and microscopic strain hardening in F.C.C. polycrystals, Acta Metall. 32 (1984) 1637–1653. doi:10.1016/0001-6160(84)90222-0.

[39] C. Tomé, G.R. Canova, U.F. Kocks, N. Christodoulou, J.J. Jonas, The relation between macroscopic and microscopic strain hardening in F.C.C. polycrystals, Acta Metall. 32 (1984) 1637–1653.

[40] J.W. Christian, S. Mahajan, Deformation twinning, Prog. Mater. Sci. 39 (1995) 1–157.

[41] S. Mishra, K. Narasimhan, I. Samajdar, Deformation twinning in AISI 316L austenitic stainless steel: role of strain and strain path, Mater. Sci. Technol. 23 (2007) 1118–1126. doi:10.1179/174328407X213242.

[42] S.K. Sahoo, V.D. Hiwarkar, I. Samajdar, P. Pant, G.K. Dey, D. Srivastav, R. Tewari, S. Banerjee, Deformation twinning in zircaloy 2, Mater. Sci. Technol. 26 (2010) 104–114. doi:10.1179/174328408X393396.

[43] D.A. Wigley, Mechanical Properties of Materials at Low Temperatures, Plenum Press,

New York-London, 1971.

[44] P. Haasen, Plastic deformation of nickel single crystals at low temperatures, Philos. Mag. 3 (1958) 384–418.

[45] U.F. Kocks, A.S. Argon, M.F. Ashby, Thermodynamics and Kinetics of Slip, Pergamon Press, 1975. doi:10.1017/CBO9781107415324.004.

[46] J.L. Derep, S. Ibrahim, R. Rouby, G. Fantozzi, Deformation behaviour of zircaloy-4 between 77 and 900 K, Acta Metall. 28 (1980) 607–619. doi:10.1016/0001-6160(80)90127-3.

[47] G. Schoeck, The activation energy of dislocation movement, Phys. Status Solidi (b). 8 (1965) 499–507. doi:10.1002/pssb.19650080209.

[48] W.R. Tyson, Strengthening of hcp Zr, Ti and Hf by interstitial solutes – a review, Can. Metall. Q. 6 (1967) 301–332. doi:10.1179/cmq.1967.6.4.301.

[49] D. Mills, G.B. Craig, The plastic deformation of zirconium–oxygen alloy single crystals in the range 77 to 950 K, Trans. AIME. 242 (1968) 1881–1890. doi:10.1017/CBO9781107415324.004.

[50] P. Das Gupta, V.S. Arunachalam, Thermally activated deformation in dilute zirconium/oxygen alloys, J. Mater. Sci. 3 (1968) 271–281. doi:10.1007/BF00741961.

[51] P. Soo, G.T. Higgins, The deformation of zirconium-hydrogen alloys, Acta Metall. 16 (1968) 187–193. doi:10.1016/0001-6160(68)90114-4.

[52] D.H. Sastry, M.J. Luton, J.J. Jonas, Thermally activated flow of H.C.P. metals at low temperatures, Phys. Status Solidi (a). 33 (1976) 173–187. doi:10.1002/pssa.2210330118.

[53] A. Akhtar, Prismatic slip in zirconium single crystals at elevated temperatures, Metall. Trans. A. 6 (1975) 1217–1222. doi:10.1007/BF02658531.

[54] D. Caillard, M. Rautenberg, X. Feaugas, Dislocation mechanisms in a zirconium alloy in the high-temperature regime: An in situ TEM investigation, Acta Mater. 87 (2015) 283–292. doi:10.1016/j.actamat.2015.01.016.

Table 1: Chemical composition of single-phase Zircaloy-4 rolled and fully recrystallized sheet used in the present study.

Elements	Sn (wt. %)	Fe (wt.%)	Cr (wt.%)	Al (ppm)	Hf (ppm)	C (ppm)	Zr
	1.5	0.22	0.1	39.0	<50	<55	Balance

Table 2: Parameters describing the evolution of threshold stress with deformation for the deformation modes at 298 K. The latent hardening parameters for grain bulk modes with grain boundary modes is zero.

System(s)	τ_0 (MPa)	τ_1 (MPa)	θ_0 (MPa)	θ_1 (MPa)	Self-hard h^{ss}	Latent hardening			
						$h^{s\ pr}$	$h^{s\ pyr}$	$h^{s\ ttw1}$	$h^{s\ ttw2}$
Prismatic $\{10\bar{1}0\}\langle\bar{1}2\bar{1}0\rangle$	50	30	1500	150	1	1	1	0	0
Pyramidal $\{10\bar{1}1\}\langle\bar{1}\bar{1}23\rangle$	315	75	3000	150	1	1	1	0	1
Extension twinning $\{10\bar{1}2\}\langle\bar{1}011\rangle$	300	1	175	175	1	1	1	10	1
Extension twinning $\{11\bar{2}1\}\langle\bar{1}\bar{1}26\rangle$	450	1	500	500	1	1	1	0	1
Grain Boundary Accommodation	250	75	3000	150	1	0	0	0	0

Table 3: Voce hardening and grain boundary accommodation parameters with respect to room temperature (298 K) at 123 K, 203 K, 298 K and 623 K for RD and TD specimens.

Temperature (K)	Voce Hardening Parameters	Grain Boundary Accommodation
123	x1.65	x2.1
203	x1.35	x1.55
298	x1	x1
623	x0.45	x0.4

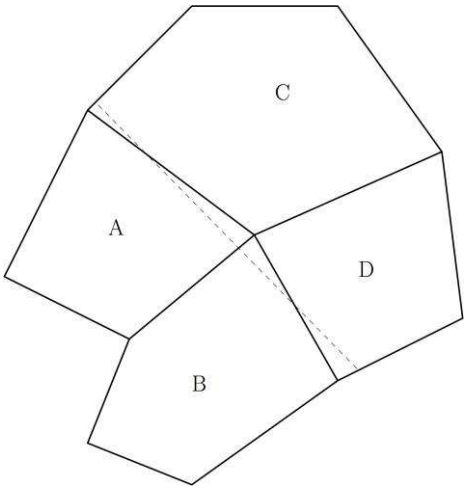

(a)

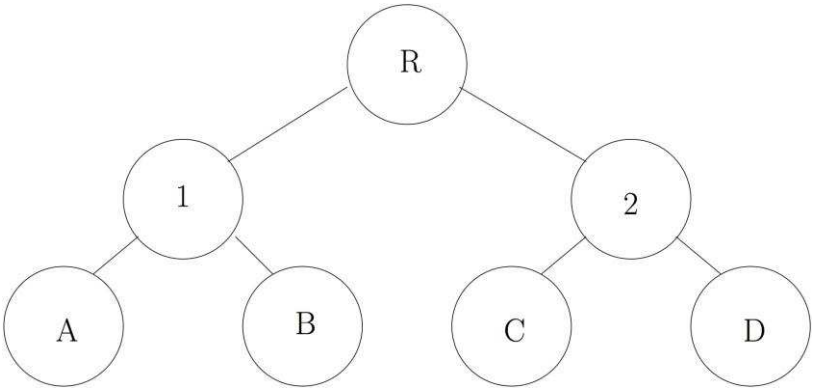

(b)

Figure 1: Binary tree based model [26] of a schematic 4-grain microstructure. (a) Idealized microstructure; (b) Balanced binary tree representation of (a).

Temp. (K)	RD	TD
Undef	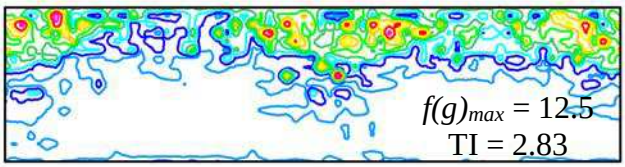	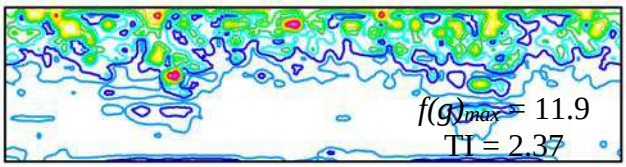
123	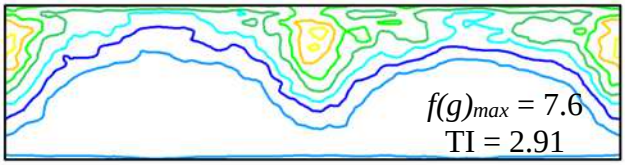	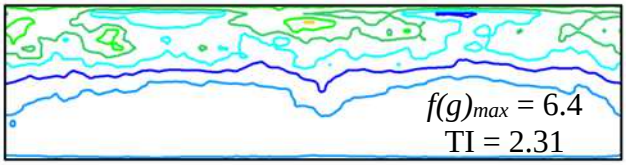
203	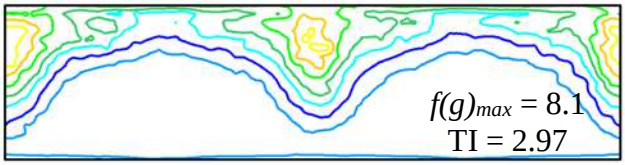	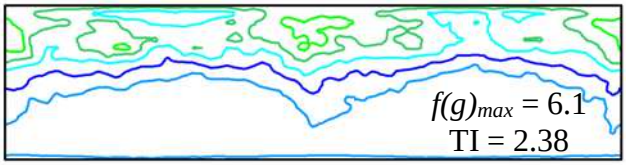
298	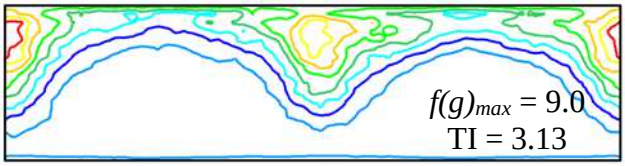	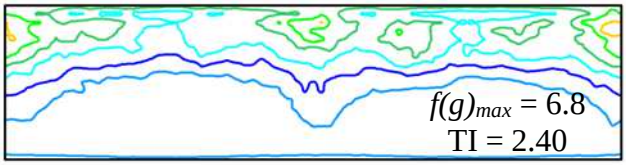
623	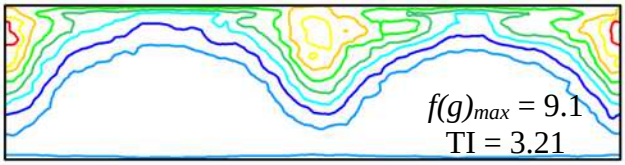	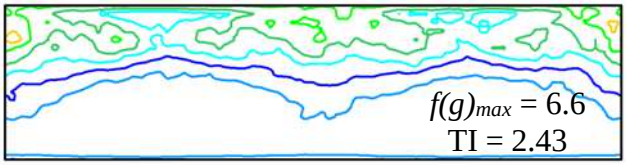

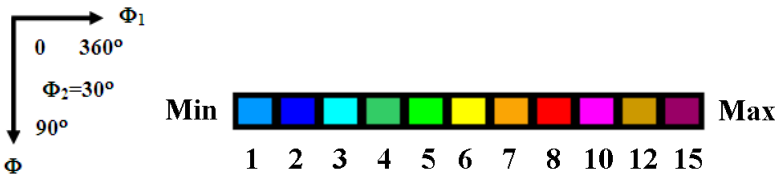

Figure 2: Post tensile deformation texture developments. Measurements were obtained at the end of tensile deformation and are shown as $\varphi_2 = 30°$ ODF sections. The RD and TD samples were subjected to 123 K, 203 K, 298 K and 623 K tensile deformation. (*For representation of color, reader may refer the web version of the paper*).

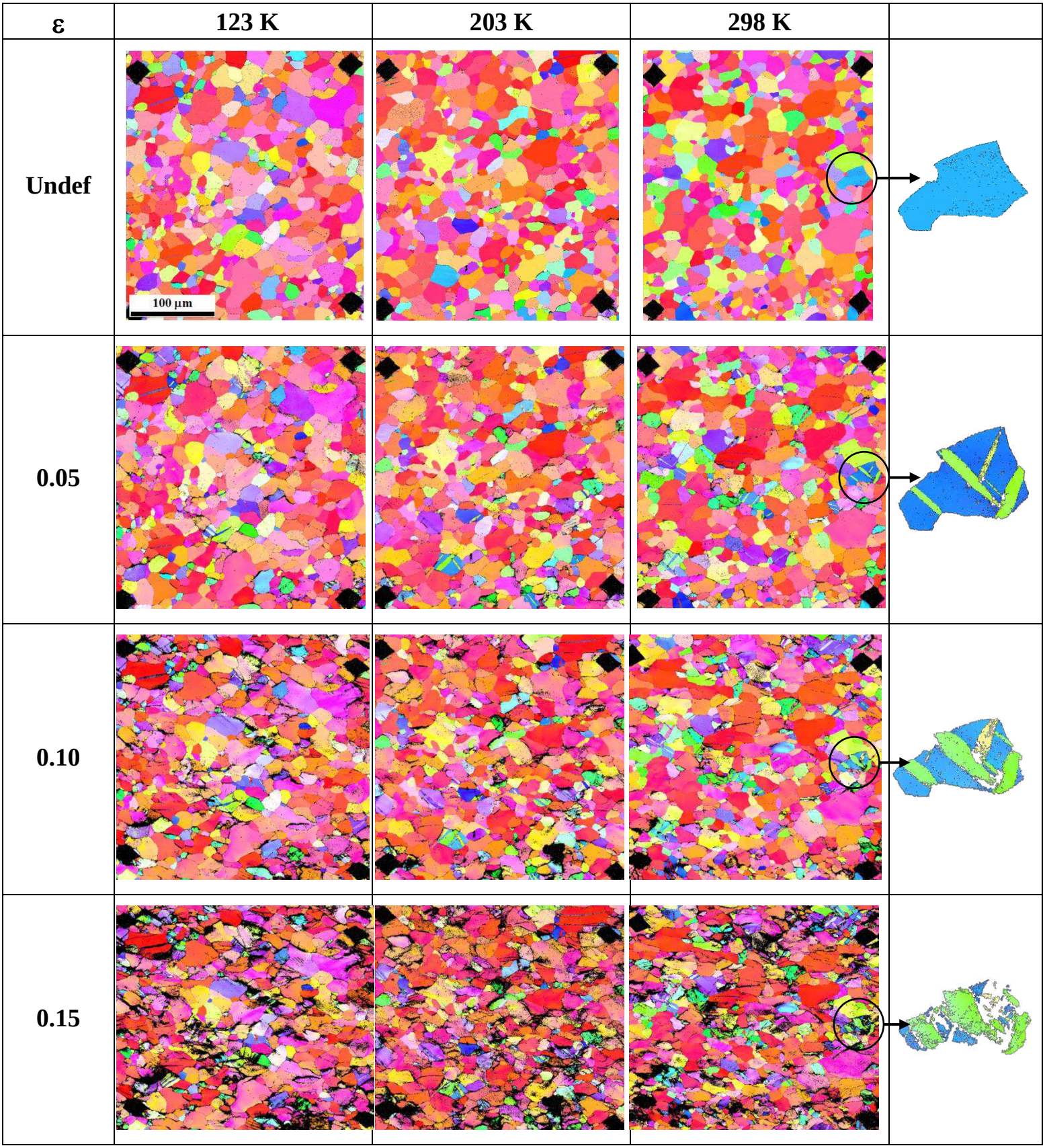

(a)

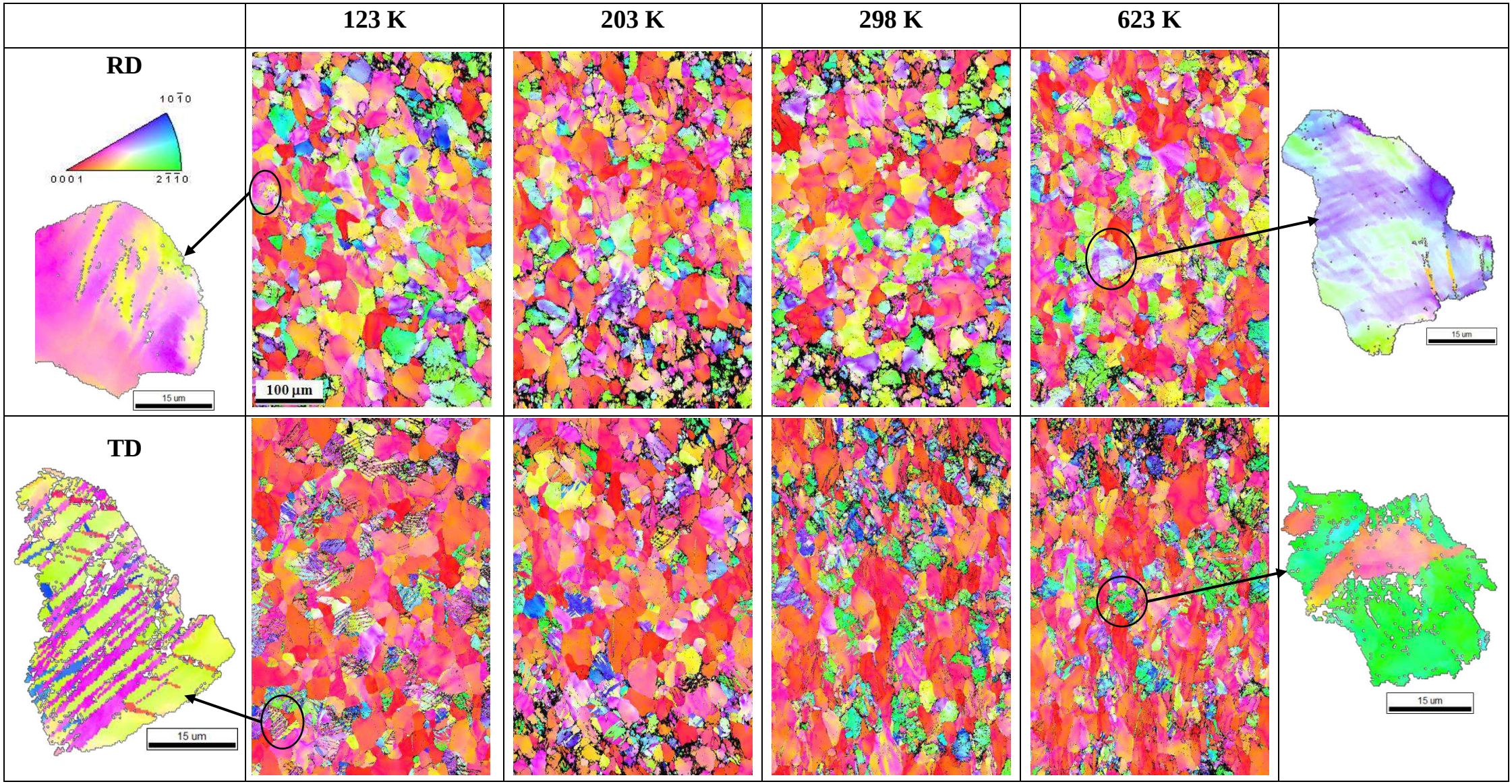

(b)

Figure 3: EBSD (electron backscattered diffraction) IPF (inverse pole figure) maps of (a) TD specimens after progressive tensile strains of 0.05, 0.1 and 0.15. These were obtained from ex-situ direct observations at 123 K, 203 K and 298 K. (b) IPF maps of RD and TD specimens after 0.25 tensile strain. Working temperatures of 123 K, 203 K, 298 K and 623 K were used to make these statistical (indirect) observation. In (a) and (b), highlighted regions are shown to describe the twin morphology. (*For representation of color, reader may refer the web version of the paper*).

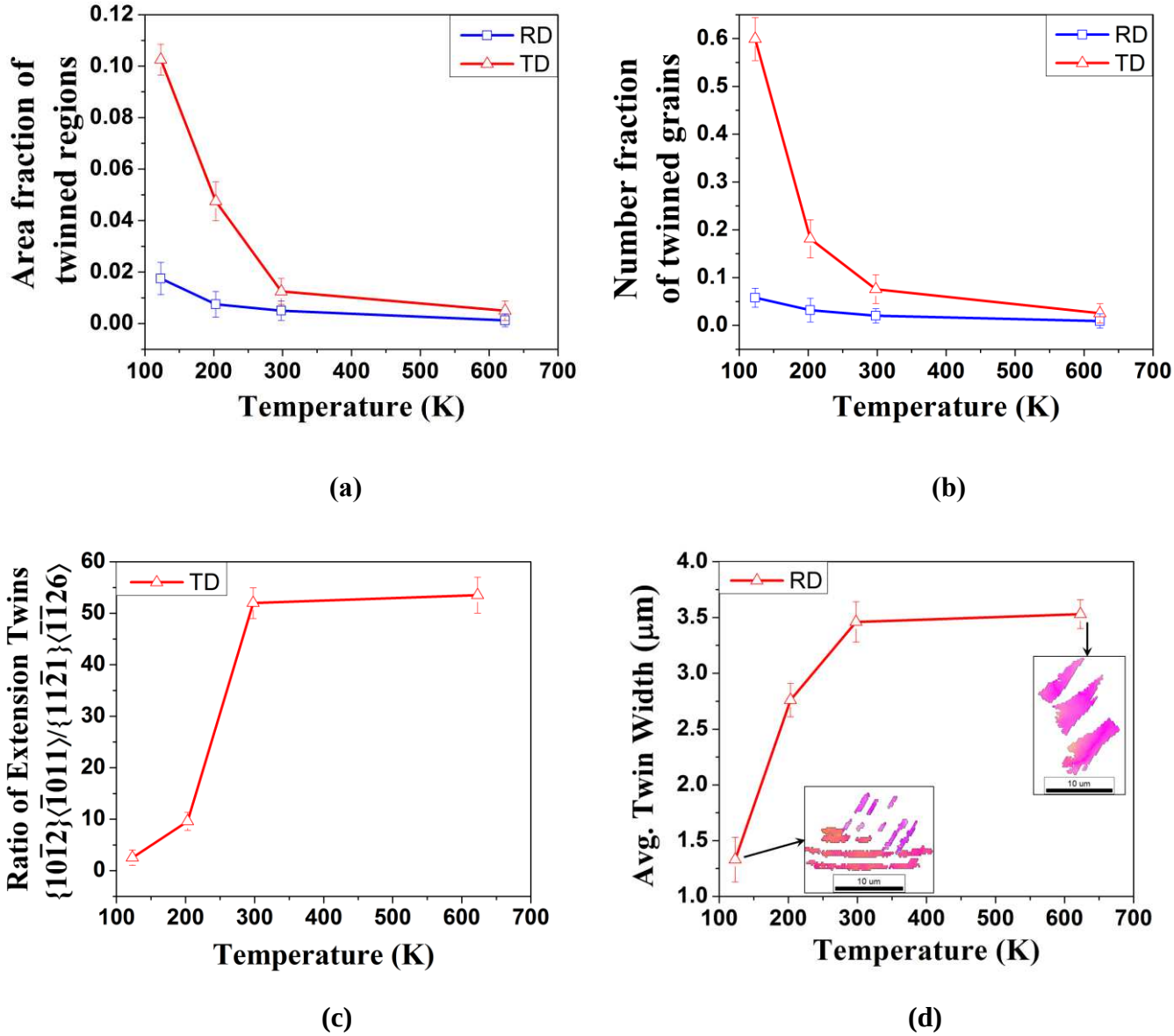

Figure 4: (a) Area fraction of twinned grains at the end of the tensile deformation at four temperatures (123 K, 203 K, 298 K and 623 K). Twins were identified manually, as automatic determination based on the axis/misorientation relationship tends to undercount twins. (b) Number fraction of twinned grains. (c) Ratio of the measured area fraction of the two extension twinning types. (d) Average width of the visible twinning regions.

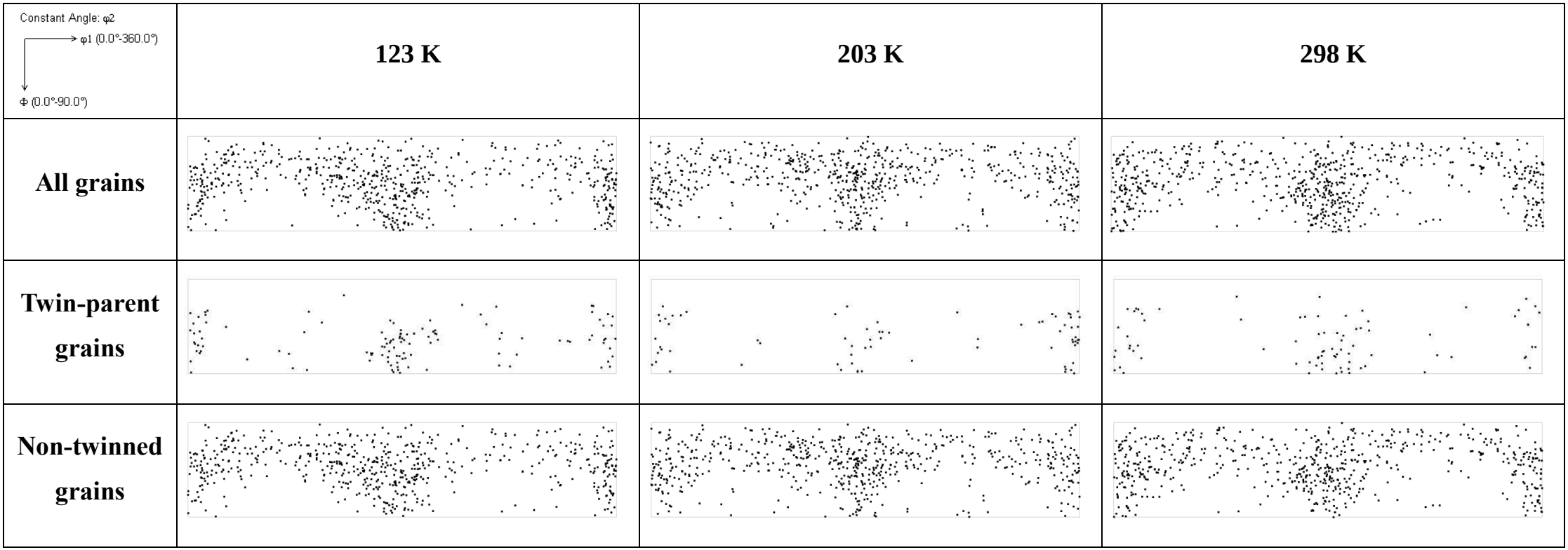

Figure 5: Euler space maps representing all, twin-parent and non-twinned grains. The data is from TD specimens, subjected to 0.15 true strain and different working temperatures 123 K, 203 K and 298 K.

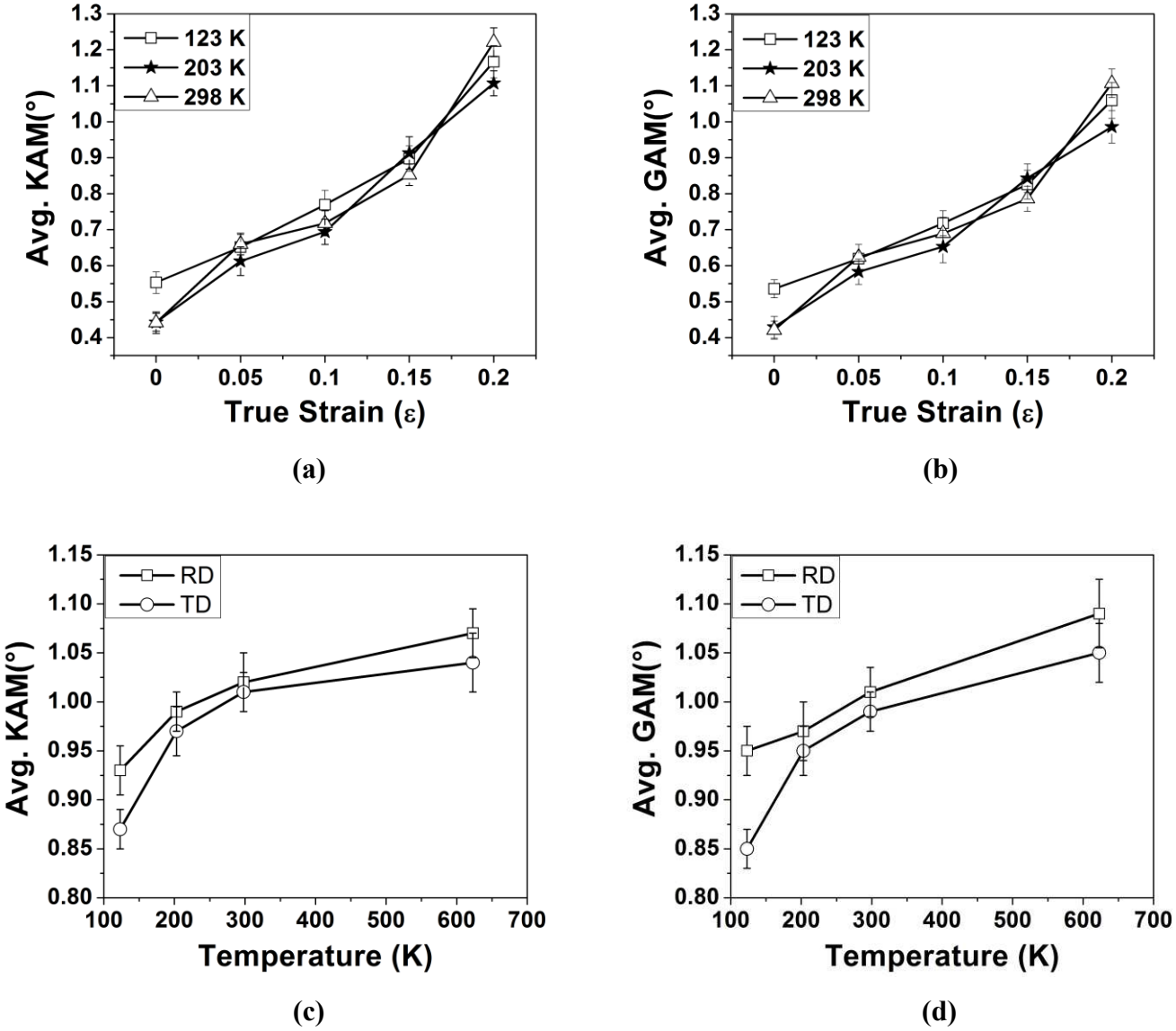

Figure 6: Measured (a) kernel average misorientation (KAM) and (b) grain average misorientation (GAM) in TD specimens. The data were obtained from direct (ex-situ) observations (Figure 3(a)) and covers a working temperature range of 123 K to 298 K. Data from indirect observations, in RD and TD specimens, showing (c) KAM and (d) GAM. (c) and (d) correspond to 0.25 tensile strain and the entire range of working temperatures 123 K to 623 K).

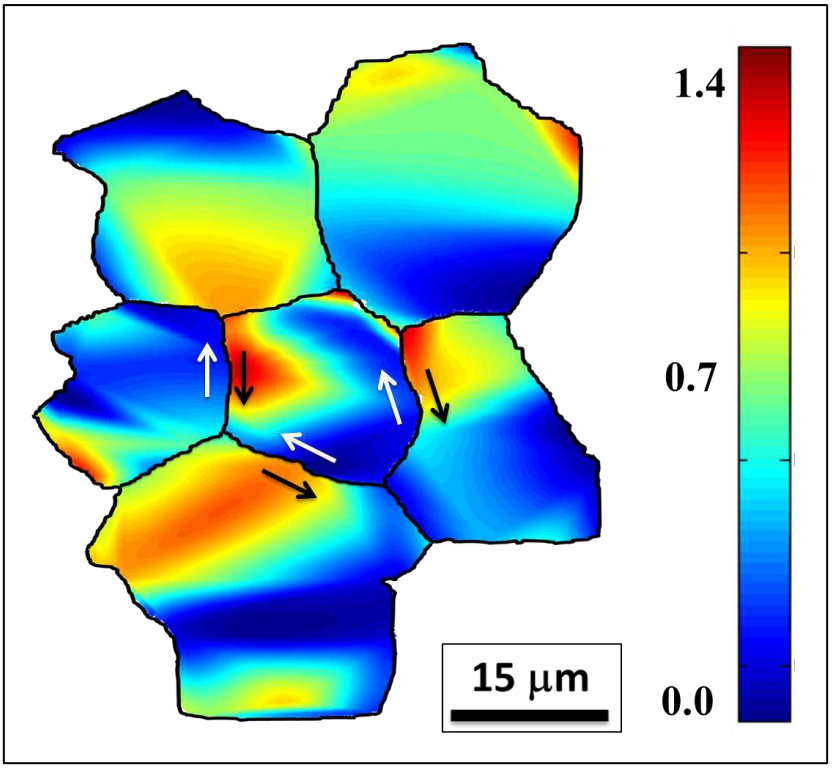

(a)

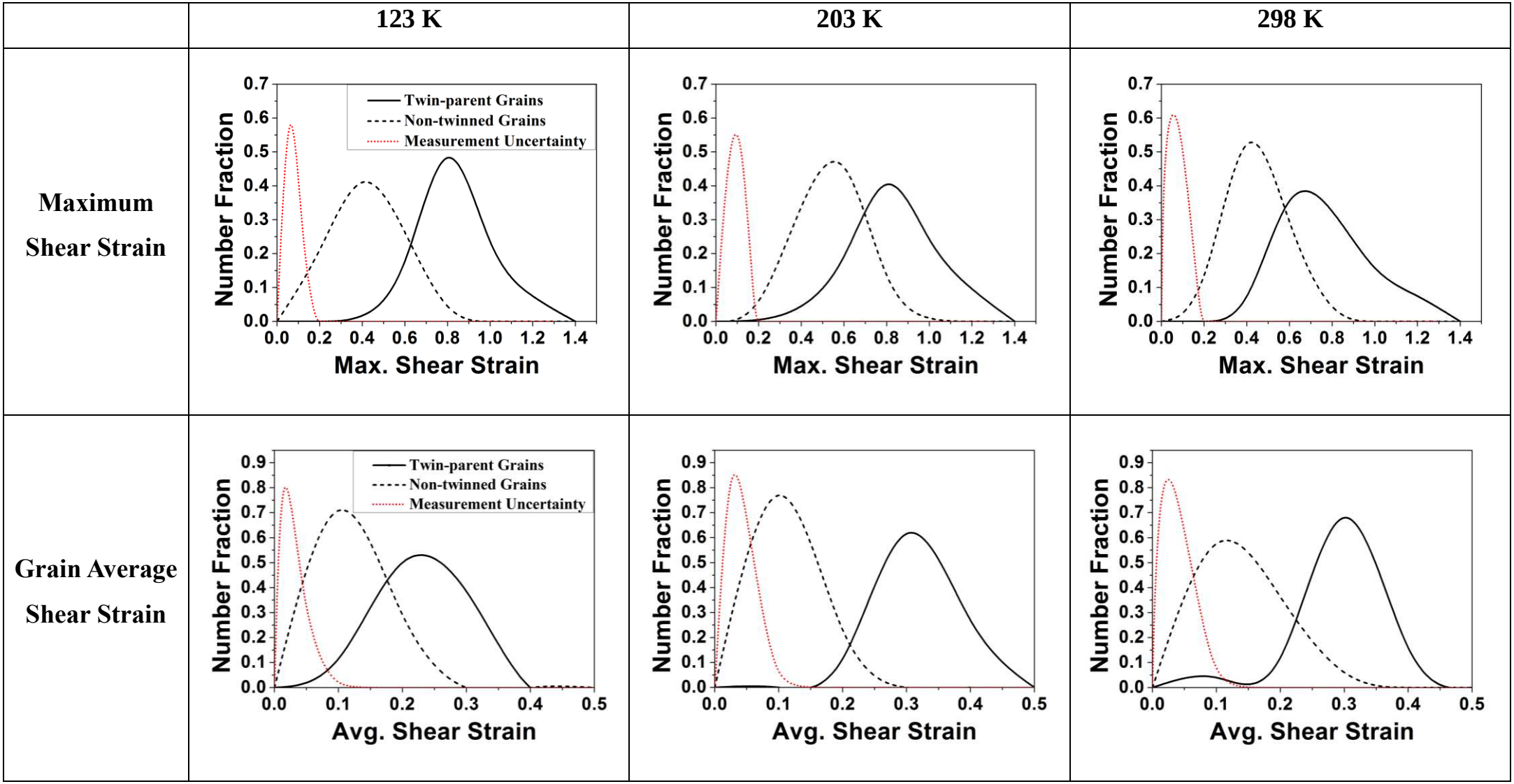

(b)

Figure 7: Near boundary mesoscopic shear (NBMS) strains were measured [34] from EBSD maps. (a) A grain cluster after ε = 0.05 at 123 K. Arrowheads are used to show positive and negative shear directions. (b) Maximum and average NBMS for twin-parent and non-twinned grains. NBMS values were obtained after an imposed tensile strain of 0.1 (direct observations with working temperatures of range of 123 K to 298 K).

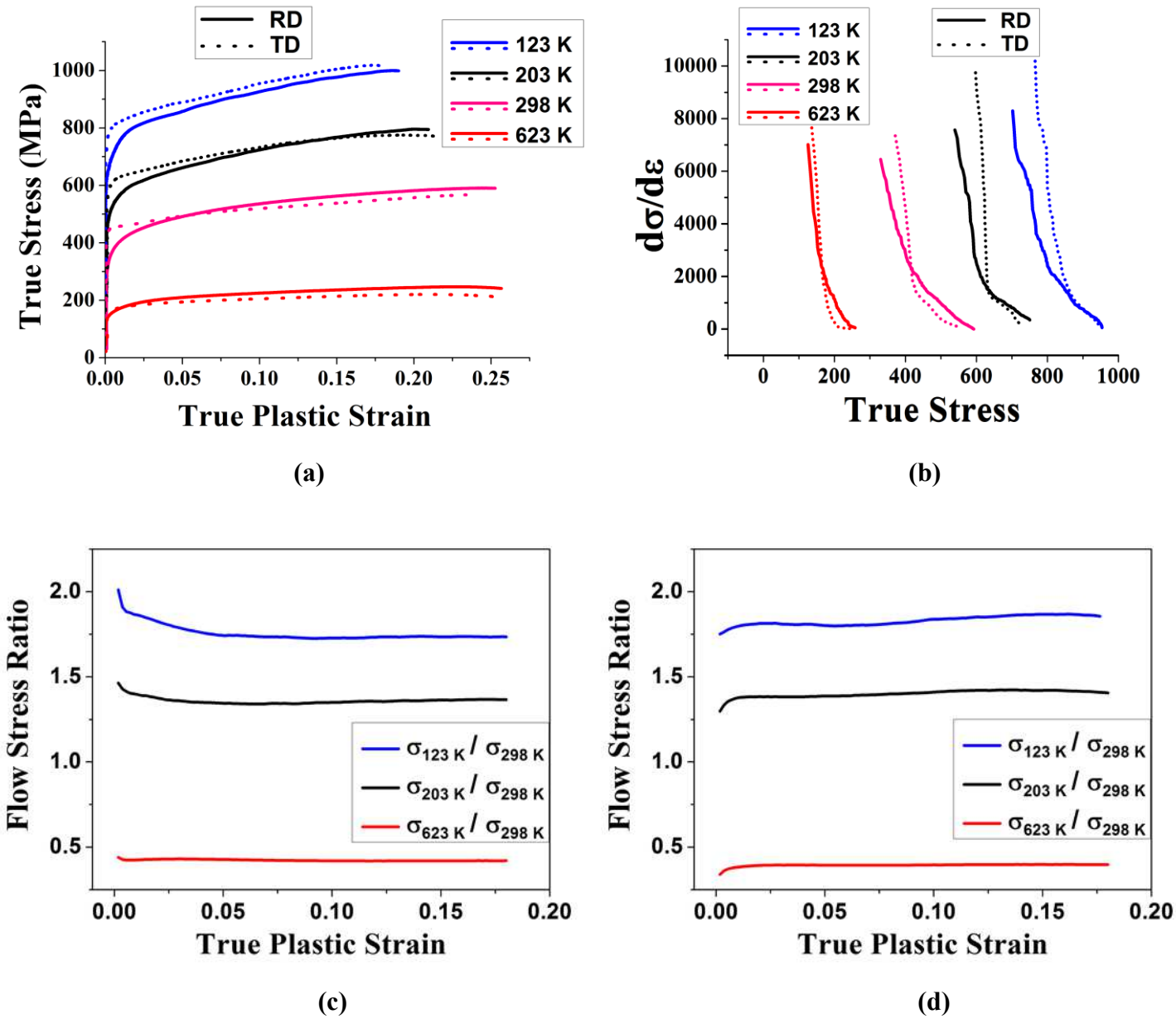

Figure 8: (a) Experimentally measured flow stress evolution with deformation at different temperatures in specimen subjected to uniaxial tension along rolling direction (RD) and along transverse direction (TD). σ denotes the true stress and ε the true plastic strain. (b) Evolution of the work hardening rate $\left(\frac{d\sigma}{d\varepsilon}\right)$ with stress derived from (a). Flow stress ratio obtained by normalizing the measured flow stress in (a) with respect to the flow stress at the same plastic strain (ε) measured at 298 K in (c) RD and (d) TD specimen.

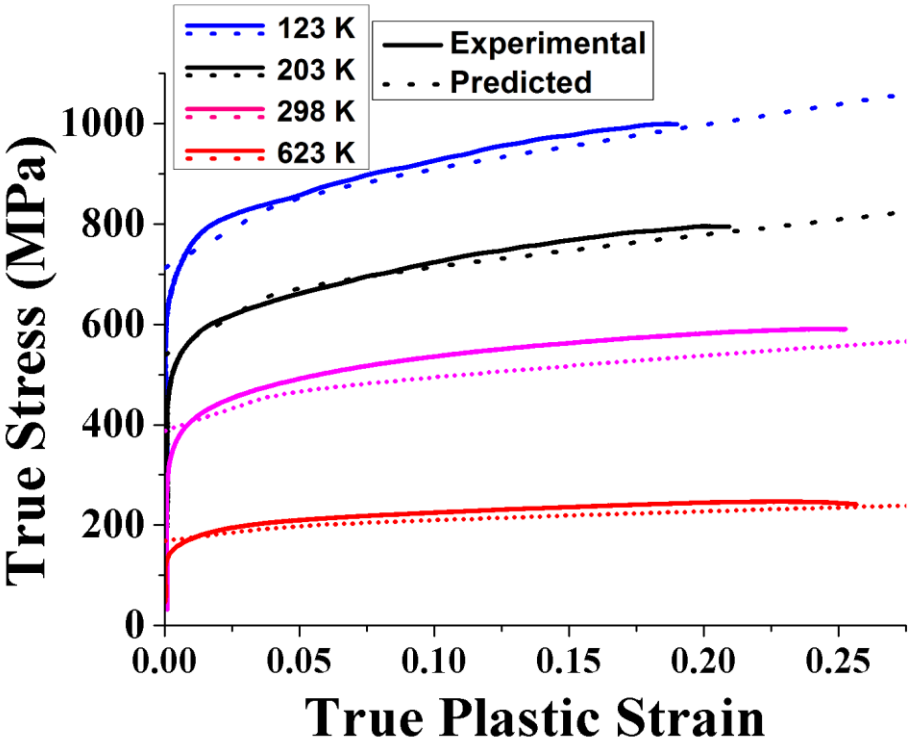
123 K
203 K
298 K
623 K
Experimental
Predicted
True Stress (MPa)
True Plastic Strain
0
200
400
600
800
1000
0.00
0.05
0.10
0.15
0.20
0.25

(a)

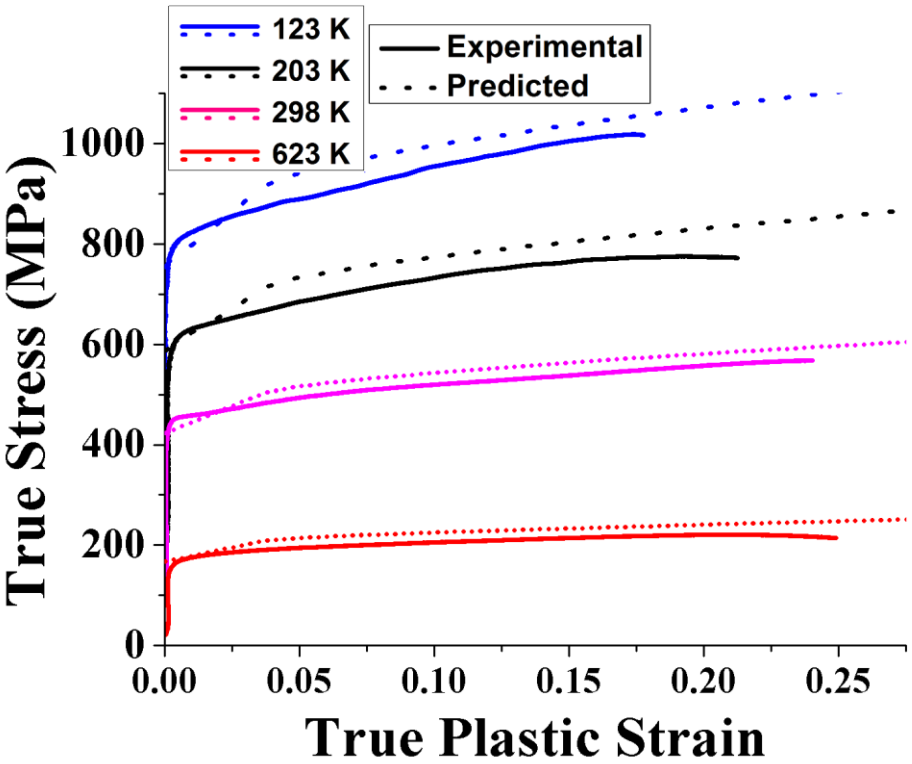
123 K
203 K
298 K
623 K
Experimental
Predicted
True Stress (MPa)
True Plastic Strain
0
200
400
600
800
1000
0.00
0.05
0.10
0.15
0.20
0.25

(b)

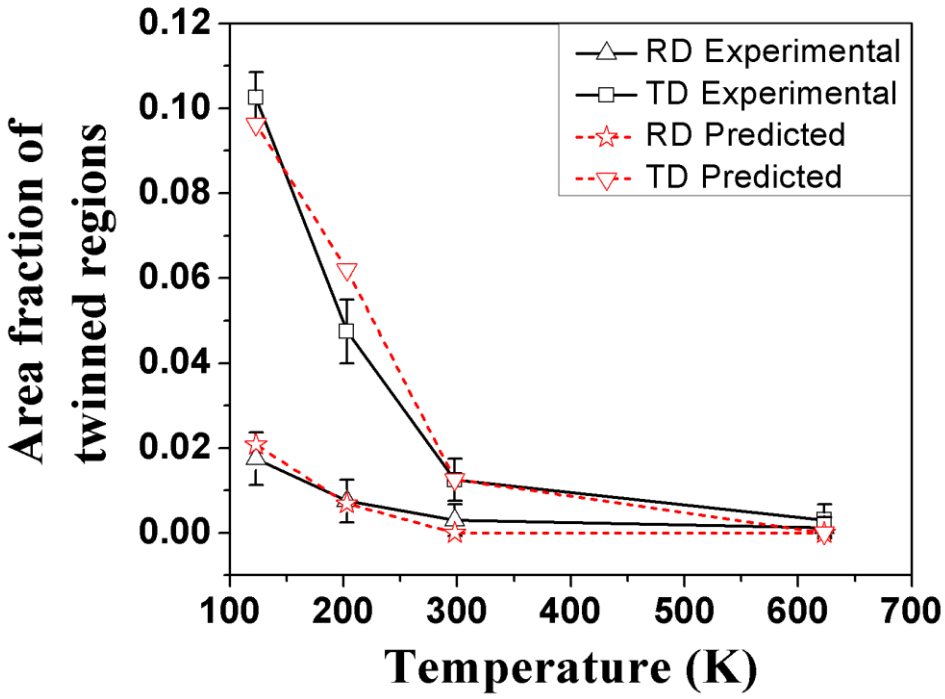

(c)

Figure 9: Experimental and predicted true stress-true plastic strain (σ-ε) behavior (a) RD, (b) TD and (c) final twin area fraction for RD and TD specimens at 123 K, 203 K, 298 K and 623 K.

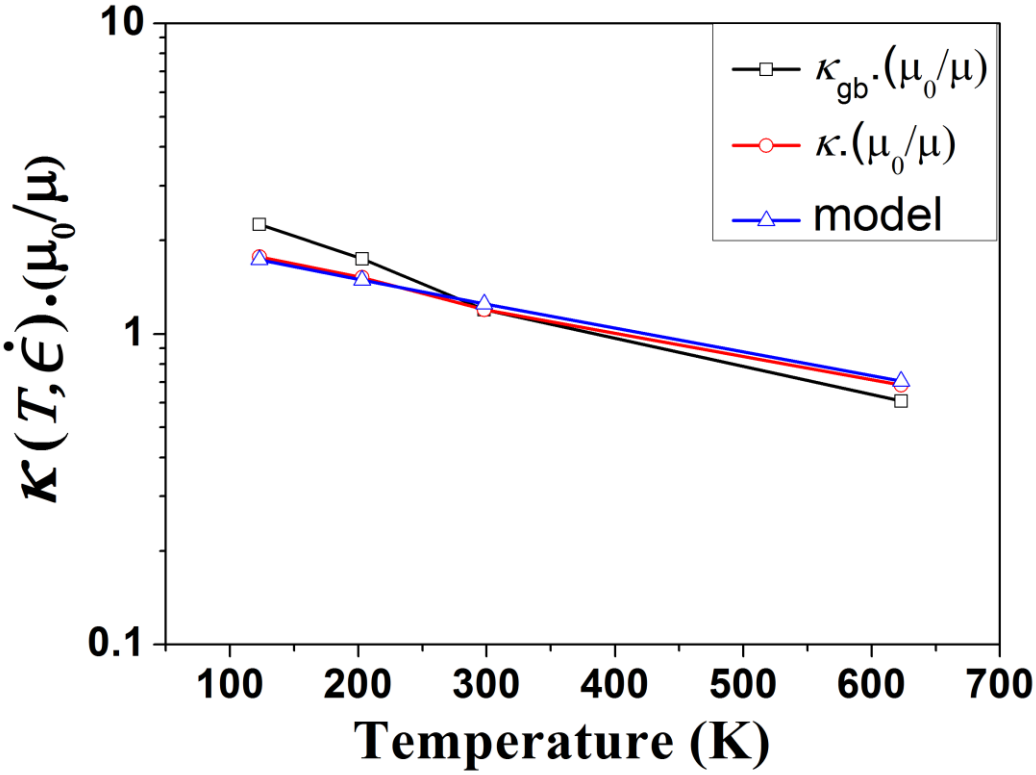

Figure 10: Temperature variation of $\kappa(T, \dot{\epsilon})$ at constant strain-rate $\dot{\epsilon} = 2 \times 10^{-5}\ /s$.

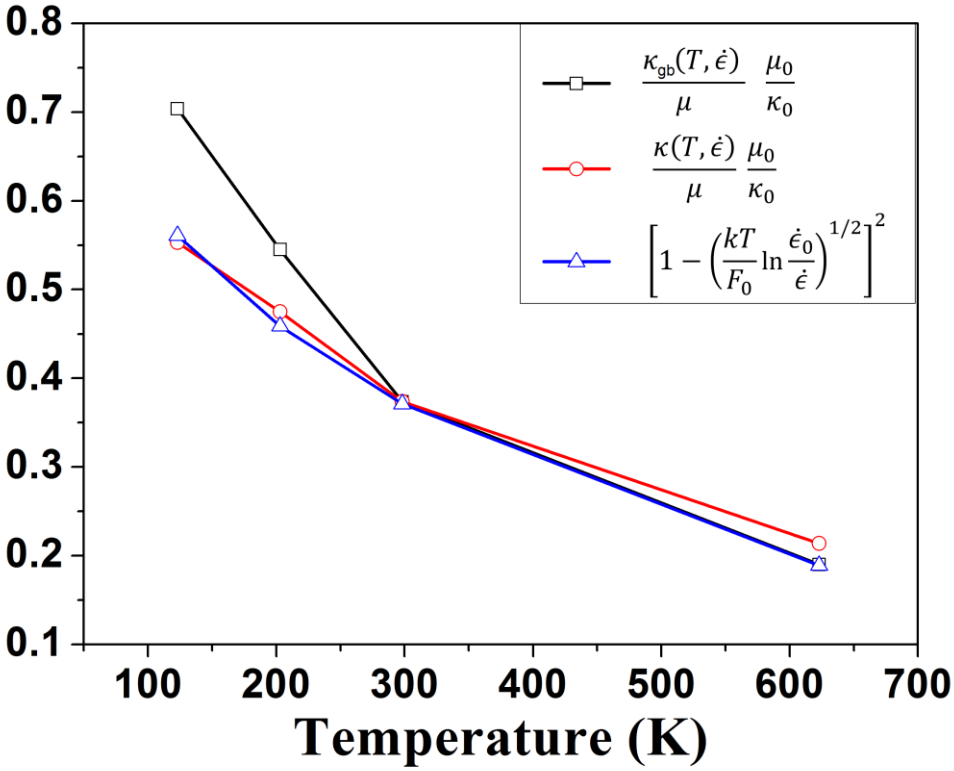

Figure 11: Variation of the left hand side and right hand side of Eq. (17) with temperature.